JOURNAL OF GEOPHYSICAL RESEARCH, VOL. 106, NO. B10, PAGES 22,051–22,066, OCTOBER 10, 2001

An integrated mechanical model of the San Andreas fault in central and northern California

Jean Chéry

Laboratoire de Géophysique, Tectonique et Sédimentologie, Université de Montpellier II Montpellier, France

Mark D. Zoback

Department of Geophysics, Stanford University, Stanford, California, USA

Riad Hassani

Laboratoire d'Instrumentation Géophysique, Université de Savoie, Le Bourget-du-Lac, France

Abstract. Several lines of evidence support the general view of the San Andreas fault system (SAFS) as a major lithospheric weakness in a generally transpressive plate margin setting. However, the influence of the weakness of the SAFS on the observed stress and deformation fields is not straightforward because factors such as interactions between the brittle upper crust and ductile lower crust, lateral fault strength variation, and the amount of convergence may all be important. The goal of this study is to model steady state deformation, relative fault-parallel velocity, and crustal stress orientations in central and northern California using realistic rheologies and boundary conditions. Using a simplified three-dimensional (3-D) finite element analysis in large strain, we model the SAFS in 2-D cross sections with no stress or strain variations along strike. We investigate the influence of different parameters such as the frictional properties of the fault zone and the adjacent crust, the viscous properties of the lower crust as determined by its thermal structure, and the thermal structure of the lithosphere. Our model appears to provide a good conceptual framework for some first-order aspects of actively deforming plate margins such as the SAFS. The following findings emerge from a variety of numerical experiments: (1) The difference in the manner of transpressive strain partitioning in central and northern California can be explained by different fault strengths and the manner in which heat flow varies with distance from the fault. (2) Only the combination of a weak fault (with an effective friction coefficient of ≈ 0.1) and a strong lateral heat flow variation predicts approximately correct stress directions in the crust adjacent to the SAFS.

1. Introduction

The goal of this study is to use a three-dimensional (3-D) mechanical model to examine the links between the rheological properties of the upper lithosphere and the behavior of the San Andreas fault system (SAFS) as constrained by observations of relative plate velocities across the SAFS, crustal stress directions, and heat flow. We assume that the SAFS is driven by lateral forces that result from the differential velocity between the Pacific plate and the North American plate. We use the differential plate velocity [*DeMets et al.*, 1990] and, more specifically, the differential velocity between the Pacific plate and the Great Valley [*Lisowski et al.*, 1991] as a velocity boundary condition in our model. Assuming that the deformation of the SAFS is controlled by the rheological state of the crust and of the fault zone, we also use heat flow data [*Lachenbruch and Sass*, 1980] and laboratory-derived constitutive laws for crustal rocks [e.g., *Byerlee*, 1978; *Brace and Kohlstedt*, 1980] as primary constraints for crustal strength of the SAFS. The San Andreas fault is assumed to have low frictional strength, both in an absolute sense, as indicated by heat flow data [*Brune et al.*, 1969; *Lachenbruch and Sass*, 1973], and in a relative sense with respect to the surrounding crust [e.g., *Zoback et al.*, 1987; *Mount and Suppe*, 1987; *Rice*, 1992]. The theoretical stress and strain fields resulting from this model are then compared to the distribution of relative plate motions, crustal deformation, and stress orientations observed in the central and northern parts of the SAFS.

Paper number 2001JB000382.
0148-0227/01/2001JB000382$09.00.

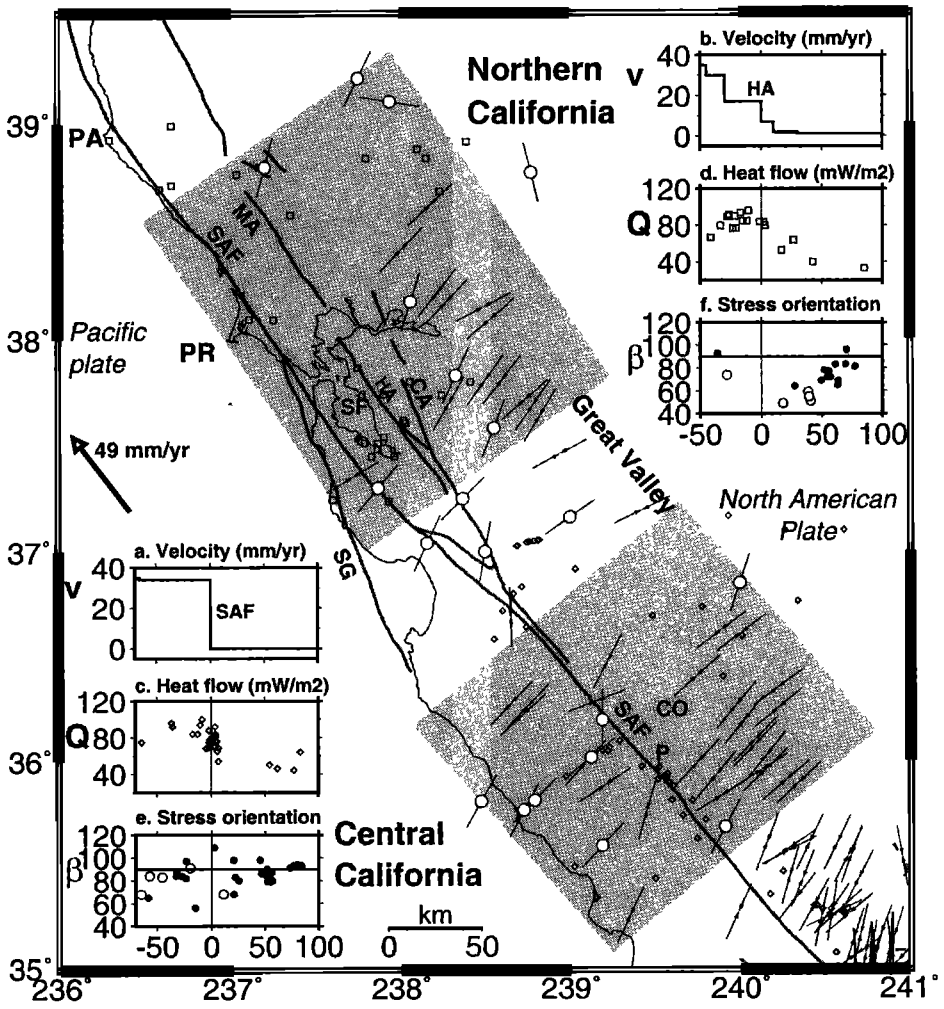

Figure 1. Tectonic map for central and northern California, with active faults (thick grey lines), heat flow data location (squares and diamonds), maximum horizontal stress orientation from borehole breakouts (inward pointing arrows) and from focal mechanisms inversions (circled lines). Insets a and b show fault-parallel velocity profiles with respect to the Great Valley based on long-term slip rates as proposed by *Thatcher and England* [1998] and *Brown* [1990]. Insets c and d show heat flow data Q (squares and diamonds) provided by the U.S. Geological Survey (courtesy C. Williams). Insets e and f: maximum horizontal stress orientation β with respect to fault direction given by borehole breakouts (solid dots) and from focal mechanisms inversions (circles). Here β and Q are plotted with respect to the distance of the Hayward-Maacama faults in northern California and with respect to the distance of the San Andreas fault in central California. PA, Point Arena; PR, Point Reyes; SF, San Fransisco; CO, Coalinga; P, Parkfield. Faults names: SAF, San Andreas; MA, Maacama; CA, Calaveras; HA, Hayward; SG, San Gregorio.

1.1. Deformation Field of the SAFS

The SAFS in central and northern California is a complex of faults that accommodate the relative motion between the Pacific plate and the North American plate (Figure 1). This system began to develop 15 Myr ago in response to the northward migration of the Mendocino triple junction [*Atwater*, 1970]. A 8°–10°clockwise rotation of the Pacific plate at $\approx$ 8 Ma changed the tectonic regime from slightly transtensional to slightly transpressional [*Atwater and Stock*, 1998]. In the following, we use the term transpression to mean that there is component compressive deformation (crustal shortening) normal to the SAFS in the area of interest. This compression results from the fact that the relative velocity vector of the Pacific plate with respect to the North American plate is slightly oblique to the strike of the SAFS. In the area of study we denote as central California in Figure 1 the average strike of the San Andreas is $\approx$ N42°W, $\approx$ 10°–12°westward of the plate motion vector at this latitude [*Argus and Gordon*, 1991]. In the area we denote as northern California in Figure 1 the average trend of the San Andreas, Hayward, and Maacama faults is $\approx$ N35°W, which is closer to the relative plate motion direction. Thus the overall

deformation field is somewhat less transpressive in this area (see discussion by *Zoback et al.* [1999]).

The present-day strike-slip component of motion between the stable North American plate (i.e., the Colorado plateau) and the Pacific plate is estimated to be 49 mm yr^{-1} [*DeMets et al.*, 1990]. Geodetic studies indicate that as much as one fourth of this relative motion is absorbed within the Basin and Range province to the east [*Dixon et al.*, 1995; *Thatcher et al.*, 1999]. As the Sierra Nevada and Great Valley crustal blocks seem to behave rigidly, the SAFS itself accommodates a strike-slip differential motion of $\approx$ 35 mm/yr.

Neotectonic studies of the SAFS show a different pattern of strain distribution in central and northern California [*Brown*, 1990]. In central California, the long-term strike-slip motion is almost completely restricted to the San Andreas Fault (SAF) itself (Figure 1, inset a), whereas in northern California, strike-slip motion is distributed among three to four subparallel faults (Figure 1, inset b) . As a consequence, the maximum slip rate along the San Francisco segment of the SAF is only $\approx$ 17 mm yr^{-1}, with an additional 15 mm yr^{-1} of slip occurring on the Hayward and Calaveras faults to the east and a few mm yr^{-1} occurring on the San Gregorio fault to the west [*USGS Working Group*, 1996; *Thatcher and England*, 1998]. The rate of contraction across the SAFS is one order of magnitude smaller than the fault parallel motion. Estimates of the shortening rate across the SAFS range between 0 and 3 mm yr^{-1}, estimated from geological reconstructions [*Thompson*, 1999] and direct geodetic measurements [*Gordon and Argus*, 1998]. Uplift rates associated with this mild convergence are variable, with average values of 0.1–0.2 mm yr^{-1} and peak values of 1–2 mm yr^{-1} where the SAFS is more oblique to the plate motion [*Brown*, 1990]. One question we address is how the overall SAFS accommodates the combination of $\approx$ 35 mm yr^{-1} of pure strike motion and $\approx$ 3 mm yr^{-1} of convergence.

Two end-member models have been proposed to describe the internal deformation of the SAFS. The first one assumes that wrench deformation distributes shear strain among en echelon folds [*Wilcox et al.*, 1973; *Teyssier and Tikoff*, 1998]. As a consequence, the deformation appears to be distributed at a scale larger than the width of the folds. This view is supported by structural analysis and paleomagnetic rotations recorded in Pleistocene sediments along one fold in central California [*Miller*, 1998]. The second model assumes that the deformation is partioned between a nearly vertical strike-slip fault (such as the SAF) and parallel thrust faults that absorb the shortening of the Coast Ranges [*Zoback et al.*, 1987; *Mount and Suppe*, 1987; *Namson and Davis*, 1988]. Little deformation should occur apart from these two kinds of faults. Recent earthquakes in Central California that occurred on thrust faults essentially parallel to the SAF (Coalinga, 1983, and Kettleman Hills, 1983 and 1985) seem to support this view. While these two models seems mutually incompatible, it has been suggested that these two mechanisms could have been both active in the SAFS but at different places and times [*Miller*, 1998], reflecting its complex tectonic history [see, e.g., *Dickinson and Wernicke*, 1997]. Another question we attempt to address in this paper is the relation between the rheology of the SAFS and the development of adjacent structural features.

1.2. Heat Flow

The rheology of the lithosphere is strongly linked to its thermal state, and the heat flow of the SAFS provides a key constraint on the construction of thermomechanical models. Heat flow along the SAFS has two two primary characteristics: (1) A broad heat flow anomaly with a mean value of 80 mW m^{-2} is associated with the SAFS. Heat flow decreases markedly to the east when approaching the Great Valley, where typical values are 40 mW m^{-2}. The shape of the transition between the regions of high and low heat flow values is relatively sharp in central California and more gradual in northern California [see *Lachenbruch and Sass*, 1980] (Figure 1, insets c and d). (2) There is no narrow heat flow anomaly associated with the trace of the SAF. This has been interpretated as a low shear heating in the frictional part of the fault zone between depths of 0 and 15 km [*Brune et al.*, 1969; *Lachenbruch and Sass*, 1980]. If a coefficient of friction of 0.6-0.8 and hydrostatic pore pressure are assumed, which are typical for crystalline crust [*Townend and Zoback*, 2000], an average shear stress of $\approx$ 100 MPa for the seismogenic zone would be expected. Such a high value of shear stress would lead to a narrow heat flow anomaly of $\approx$ 60 mW m^{-2}, which is not observed. The lack of narrow heat flow anomaly, associated with the anomalous stress orientation of the SAFS, constitutes the stress/heat flow paradox of the SAF [*Lachenbruch and Sass*, 1992]. Modeling heat flow data using a conductive model for the lithosphere limits the mean value of shear stress on the seismogenic fault to be no larger than $\approx$ 20 MPa. If mechanical heat production occurs in the lower crust (or upper mantle) by viscous deformation [*Thatcher and England*, 1998], heat flow would spread over a wide zone in a manner similar to the broad heat flow anomaly previously described.

1.3. Stress

Borehole stress measurements and earthquake focal plane mechanisms are the main source of information about relative stress magnitude and orientation. In general, a high angle (β) between the direction of the maximum horizontal stress σ_H and the local fault orientation is observed along the entire length of the SAFS [e.g., *Zoback et al.*, 1987] in central California (Figure 1, inset e), where the mean value of β is 84° to the SAF even at distances as large as 70 km from the fault

[*Mount and Suppe*, 1987]. This stress orientation is consistent with recent thrust earthquakes such as Coalinga, 1983, which have occurred as pure thrust events with a fault trace parallel to the SAF. Values of β east of San Francisco bay area are less severe, with an average angle of 70° with respect to the Hayward fault (Figure 1, inset f). The fact that β generally corresponds to very high angles provides independent evidence of the weakness of the SAF. Indeed, this high angle forces the average shear stress on the fault to be smaller than 10 MPa between depths of 0 and 15 km [*Mount and Suppe*, 1987].

2. Mechanical Modeling

2.1. Previous Mechanical Modeling of the SAFS

Since the simple conceptual models of *Lachenbruch and Sass* [1973, 1980], two more detailed models of the SAFS have been developed using the finite element method (FEM). *Bird and Kong* [1994] built a relatively complete model of California lithosphere, including faults of different strengths and fairly realistic boundary conditions. Their mechanical formulation considered a lithosphere with layer-averaged frictional and viscous behavior and did not account explicitly for stress components in the vertical planes of the lithosphere. Their extensive parametric study found an effective coefficient of friction of 0.17 as an average value for the SAFS. *Braun and Beaumont* [1995] published the first full 3-D model of a convergent plate boundary and studied the effect of normal convergence on the tectonic style of the Californian Coast Ranges. As their model is driven by subduction at the base of the crust, it does not appear to be representative of the present-day interaction of the Pacific and North American plates as the overall convergence rate is so small [*Gordon and Argus*, 1998]. We utilize here a 3-D FEM model of the SAFS and Coast Ranges that has similar characteristics to the model of *Braun and Beaumont* [1995] to evaluate the distribution of stress and strain in vertical cross sections. Our assumptions about rheology and boundary conditions are discussed in sections 2.3 and 2.4.

2.2. Numerical Formulation

Our numerical model is based on the FEM that requires us to solve (after suitable discretization) a system of equations formed by the momentum equation, the constitutive law of the medium, and static and kinematic boundary conditions. The FEM is described in many classical books [e.g., *Zienkiewicz*, 1977; *Hinton and Owen*, 1980; *Dhatt and Thouzot*, 1981]. As some parts of our numerical model are based on specific choices that concern finite strain theory, the space and time discretization of the momentum equation, the integration of constitutive laws, and the implementation of boundary conditions, we describe these different aspects in Appendices A1–A5.

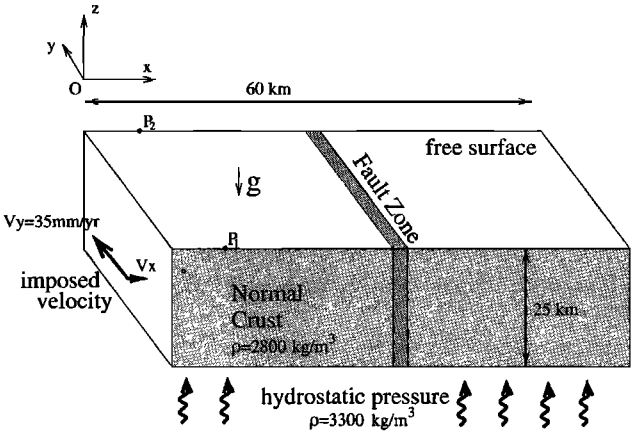

Figure 2. Geometry and boundary conditions of the mechanical model. The model has neither geometrical nor thermal variation along strike (the y direction). Model thickness in y direction is arbitrary. The left side, which corresponds to the Pacific plate, has relative velocity components V_x and V_y with respect to the right side (hidden), which corresponds to the Great Valley.

2.3. Geometry and Boundary Conditions

Our crustal model of the SAFS (Figure 2) has a width of 60 km (x) and a 25 km depth (z), following *Thompson* [1999]. We assume no initial topography. Because the vertical plane Oxz is a symmetry plane (there are no material variations along the y direction), the thickness of the 3-D finite element mesh is somewhat arbitrary. We have checked experimentally that neither the mesh thickness in the y direction nor the number of element layers in this direction has a significant effect on the numerical results. Because of the high heat flow value within the SAFS we neglect the strength of the underlying mantle and assume that the mantle acts as an inviscid fluid with a density of 3300 kg m^{-3}. As a consequence, only hydrostatic traction without shear stress occurs at the crust-mantle boundary, but horizontal and vertical motions are possible. The crustal density is assumed to be uniform (2800 kg m^{-3}), and the initial isotropic mean stress is set to be equal to the lithostatic value. We initially assume that the temperature field corresponds to a thermal gradient of 27°C km^{-1} (consistent with a value of 80 mW m^{-2} in the Coast Ranges) but we will vary this in the section 3.3. We describe the SAF as a vertical discontinuity embedded in the crust. We assume that the width of the fault is between 0.5 and 1 km (corresponding to one element size). A strike-slip velocity V_y of 35 mm yr^{-1} is applied on the left side of the fault in order to account for the Pacific plate motion with respect to the Great Valley. An initial normal velocity V_x of 3.5 mm yr^{-1} is specified to simulate a transpression. V_z is not constrained so as to allow for possible vertical motions. As the relative plate velocity vector is out of the symmetry plane Oxz, all strain and stress components are non zero and a 2-D plane strain formulation (which requires xy, yy, and yz components to be zero) cannot be used for this

analysis. A 3-D mechanical model is therefore needed as was previously used by *Braun and Beaumont* [1995].

2.4. Constitutive Laws

The basic goal of this study is to model steady state deformation, relative plate velocities, and the state of stress of the SAFS using a realistic lithospheric rheology and boundary conditions. In the elastic domain we assume a classical linear relation between the strain rate d and the stress rate tensor $\dot{\sigma}$ (Hooke law):

$$\dot{\sigma} = 2Gd + \lambda \,\mathrm{tr}(d)I, \tag{1}$$

where λ and G are the Lamé parameters, I is the identity tensor, and tr the trace of the tensor. Typical values for the crust are chosen for associated Young's modulus (10^{11} Pa) and for Poisson's ratio (0.25). In the frictional domain, this simple elastic behavior only holds for a given stress range defined by a yield criterion f such as

$$f(\sigma) < 0. \tag{2}$$

We use a Drucker-Prager model in order to model the increase of differential stress with pressure. Such a model is defined by an internal friction angle ϕ, a dilatancy angle ψ, and a cohesion c. By matching the Mohr-Coulomb model in the triaxal test [*Leroy and Ortiz*, 1989], the yield criterion can be described as follows:

$$f(\sigma) = J_2(\sigma) - \alpha(\kappa)\,[\bar{\sigma} + \frac{c}{\tan\phi}] < 0 \tag{3}$$

$$J_2(\sigma) = \sqrt{\frac{3}{2}}\,\sqrt{\mathrm{dev}\sigma : \mathrm{dev}\sigma} \tag{4}$$

$$\alpha(\kappa) = \frac{6\sin\phi(\kappa)}{3 - \sin\phi(\kappa)} \tag{5}$$

$$\bar{\sigma} = -\frac{1}{3}\,\mathrm{tr}(\sigma), \tag{6}$$

where dev is the deviatoric part of a tensor, $\bar{\sigma}$ is the mean stress, the colon represented the contracted product, and κ is a measure of the frictional strain. Additional relations are given in Appendix A1.

A viscoelastic law (linear Maxwell model) is adopted to fit the strain rate dependent "power law" rheologies:

$$\dot{\sigma} = 2G[d - \gamma\,\mathrm{dev}(\sigma)] + \lambda\,\mathrm{tr}(d)I, \tag{7}$$

where γ is a fluidity ($\mathrm{Pa}^{-1}\mathrm{s}^{-1}$) that depends on temperature T:

$$\gamma = \gamma_0\, e^{-E_a/RT}, \tag{8}$$

where E_a is the activation energy and R is the gas constant. Following the concept of strength envelopes, we assume that the lithosphere behaves as an elastoplastic medium at low temperature and as a viscoelastic medium at high temperature. Because the behavior at a given depth depends on evolving variables such as strain rate, we consider that a point in the model at a time t behaves as a viscoelastic medium unless the viscoelastic stress prediction violates the yield condition (equation (3)). In this case the medium is assumed to behave as an elastoplastic medium, and a new stress prediction is done. As a result, the elastoplastic-viscoelastic transition of the model directly reflects the variation of parameters in the constitutive laws such as temperature, stress, and strain rate.

3. Numerical Experiments

3.1. Crustal and Fault Friction

The frictional behavior of the normal crust outside the principal strike-slip fault is set in the following way. Cohesion c is set to a low value (1 MPa), which is negligible with regard to the mean level of stress in the frictional crust. The measured friction angle for most frictional material is $\approx 30°$[*Byerlee*, 1978]. However, here we need to incorporate the fact that pore pressure exists within the crust. Because the pore pressure is not present in our Drucker-Prager model, we choose to adjust the friction angle in the "normal" crust ϕ_{NC} outside the fault zone. We first express ϕ as

$$\phi = \arcsin\frac{3\alpha}{6 + \alpha}. \tag{9}$$

If we neglect the cohesion, α is given by $J_2/\bar{\sigma}$. Therefore the friction angle ϕ has a similar meaning as for Coulomb friction, as α express the maximum ratio between the deviatoric stress norm J_2 and the mean stress $\bar{\sigma}$. For a state of stress given by $\sigma_1 = 2\ \sigma_3$ and $\sigma_2 = 1.5\ \sigma_3$, we can compute that $\bar{\sigma} = 1.5\ \sigma_3$ and that $J_2 = 0.5\ \sqrt{3}\ \sigma_3$, which gives $\alpha = 1/\sqrt{3}$ and $\phi \approx 14.8°$. We will use a value of 15° for the effective friction angle ϕ_{NC} of the normal crust that corresponds to a friction coefficient of 0.6 [e.g., *Byerlee*, 1978; *Townend and Zoback*, 2000] for hydrostatic pore pressure in the normal crust.

The choice of the friction angle for the SAF is based on the assumption than the fault is weaker than the surrounding crust for the reasons cited above. We choose two values of ϕ (3° and 10°) in order to model a weak fault zone and a moderately weak fault, respectively. It is important to note that this hypothesis is different to those made by *Braun and Beaumont* [1995], which made no distinction between the strength of the crust and the fault zone.

We setup identical viscous properties of the lower crust and the fault zone beneath the brittle-ductile transition. Thus the only difference between the fault zone and normal crust is the effective friction angle ϕ. The choice of viscous parameters is done by assuming an effective viscosity of 10^{23} Pa s at 350°C. We assume an effective viscosity of 10^{20} Pa s at 650°C, in order to model the viscosity decrease in the lower crust [*Strehlau and Meissner*, 1987]. The viscous parameters that we use for the Maxwell model predict a state of stress that is in good agreement with the stress varia-

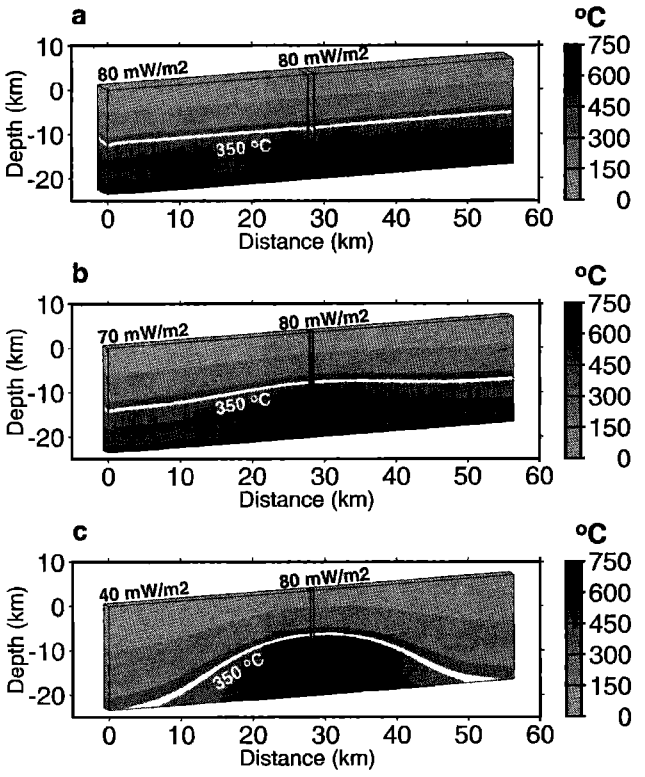

Figure 3. Three temperature fields used for cases 1 to 7. (a) No lateral heat flow variation. The value of 80 mW m^{-2} is typical to the SAF. (b) Moderate lateral heat flow variation used for case 6. (c) Strong lateral heat flow variation. The value of 40 mW m^{-2} is typical of the Great Valley.

tion derived from laboratory experiments for quartzofeldspathic rocks [e.g., *Kirby*, 1985].

3.2. Geotherms

Temperature has a major effect on the lithospheric strain as it controls the effective viscosity in the lower crust and therefore the transition between frictional behavior (brittle field) and viscous behavior (ductile field). In order to evaluate the effect of the thermal structure on the strain and stress field of the SAFS, we investigated three different temperature fields. As our mechanical analysis has a typical duration of 50,000 years, we assume the temperature field does not evolve during this period. This hypothesis is reasonable as the length scale for the diffusion of a thermal perturbation during this period of time is on the order of 1 km. The following three temperature fields were defined assuming a thermal conductivity of 3 W $m^{-1}°C^{-1}$ [*Carslaw and Jaeger*, 1959]. In all cases the 350°C isotherm approximately corresponds to the transition between frictional and viscous processes for a strain rate of 10^{-15} s^{-1}. (1) The first field is a constant surface heat flow value of 80 mW m^{-2}, which corresponds to a vertical thermal gradient of 27°C km^{-1} (Figure 3a). Note that the 350°isotherm is at 13 km depth. (2) The second field is a mild surface heat flow variation from 80 mW m^{-2} at the fault zone to 70 mW m^{-2} 30 km away from the fault (Figure 3b). In this case the 350°C isotherm is at 13 km depth near the fault and only slightly deeper away from that fault. (3) The third field is a large surface heat flow variation from 80 mW m^{-2} at the fault zone to 40 mW m^{-2} 30 km away from the fault (Figure 3c). For this last case the 350°C isotherm is at 25 km depth on both the left and right sides of the model.

3.3. Velocity, Strain, and Stress for Experimental Cases 1–5

The combination of two values of fault friction and the three different geotherms described above lead to a number of numerical experiments labeled cases 1 to

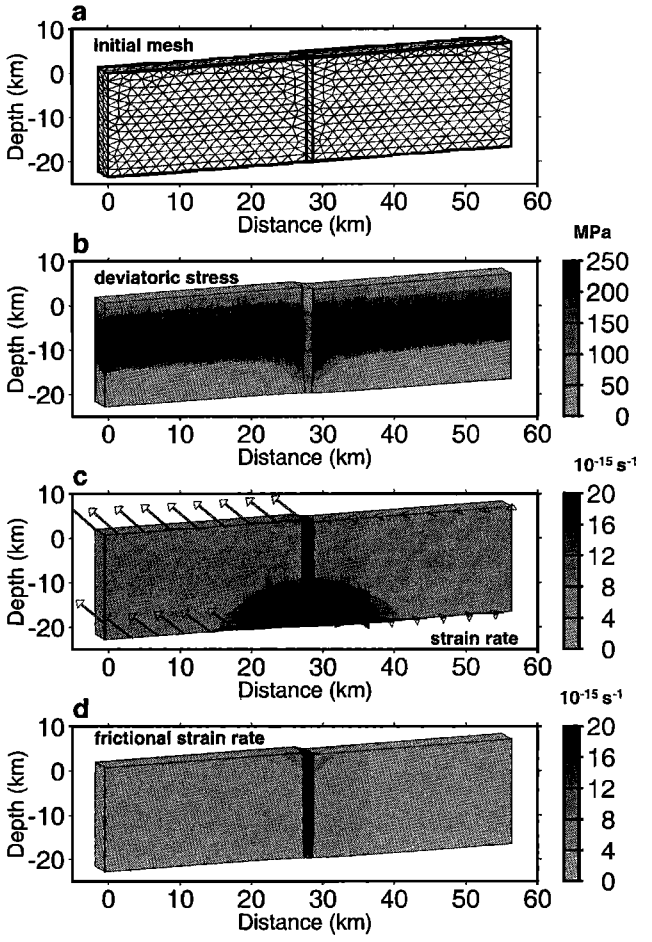

Figure 4. Stress and strain of case 1 ($\phi = 3°$ and $\eta = 10^{20}$Pa s) after 57,143 years. (a) Initial mesh (coarse mesh of 5760 elements, mesh thickness along y direction is 4 km). (b) Deviatoric stress norm $J_2(\sigma)$. Stress increase with depth in the upper crust reflects the frictional behavior. Stress decrease in the lower crust reflects the temperature-dependant viscous behavior. (c) Averaged total strain rate $\Delta I_2(d)/\Delta t$ (see (A12) for I_2). Strain rate is localized in the upper crust of the fault zone and diffuses in the lower crust below. (d) Averaged frictional strain rate $\Delta I_2(d_p)/\Delta t$ (see (A13) for d_p). Note that frictional strain develops at depth in the fault zone due to high strain rate, whereas it is negligible in the crust.

Table 1. Mechanical Parameters for Models [a]

Case	Q, mWm^{-2}	ϕ, deg	Comments
1	80	3	uniform heat flow, very weak fault
2	80	10	moderately weak fault
3	80	3	same as case 1 but the crust is decoupled
4	80-40	3	same as case 1 but marked decrease of heat flow away from the fault
5	80-40	10	same as case 4 but moderately weak fault
6	80-70	10	moderate decrease of heat flow, moderately weak fault, strain softening of the crust
7	80-40	3	same as case 4 but strain softening of the crust

[a] Q is the surface heat flow which can vary horizontally if two numbers are given; ϕ is the effective Drucker-Prager angle for the fault zone.

7 (see Table 1). The duration of each experiment corresponds to a total time of 57,143 years (20,000 time steps) in order to achieve 2 km of strike-slip displacement between the left and right sides of the model, which is enough to reach a steady state for stress and strain rate. Cases 1–3 correspond to a constant surface heat flow of 80 mW m^{-2}. Case 1 involves very low fault friction, case 2 considers a moderately weak fault, and case 3 considers a very low fault friction as well as lack of coupling between the upper and lower crust. Cases 4 and 5 consider a large lateral heat flow variation from 80 to 40 mW m^{-2} as is observed between the SAF and the Great Valley for two different values of fault strength.

Case 1 (Figure 4) should account for many of the general properties of central and northern California SAFS: a strong crust, a weak fault zone, and high heat flow. The second stress invariant $J_2(\sigma)$ (equation (4)) allows us to study the magnitude of the differential stress independent of the stress directions (Figure 4b). The crust outside the fault zone displays a linear increase of $J_2(\sigma)$ between depths of 0 and 12 km due to the increase of overburden stress. Below 12 km the rapid decay of $J_2(\sigma)$ from 300 to a few MPa is caused by high temperatures in the ductile regime. The fault zone roughly displays the same variation of J_2 but never exceeds 50 MPa. The second invariant of the strain rate $I_2(d)$ (equation (A12)) indicates that only the fault zone and the lower crust deform significantly ($> 10^{-14}$ s^{-1}) as a narrow band between 0 and 13 km depth and within a broad domain in the viscous crust below (Figure 4c). The second invariant of the frictional strain rate $I_2(d_p)$ represents only the deformation corresponding to the Drucker-Prager behavior (Figure 4d) and does not take into account the viscous strain. It therefore appears that the deformation takes place in the lower crust with two different mechanisms. The fault zone undergoes mainly a frictional deformation as deep as 24 km. By contrast, the "normal" lower crust outside the fault zone deforms viscously as the frictional strain rate $I_2(d_p)$ is close to zero outside the fault zone.

Cases 1–5 are also analyzed with respect to the surface horizontal velocity field (Figure 5) and maximum horizontal stress direction (Figure 6). When low fault zone friction is considered (cases 1, 3 and 4), velocity gradients mostly develop in the fault zone itself and are not influenced by the temperature field at depth. The

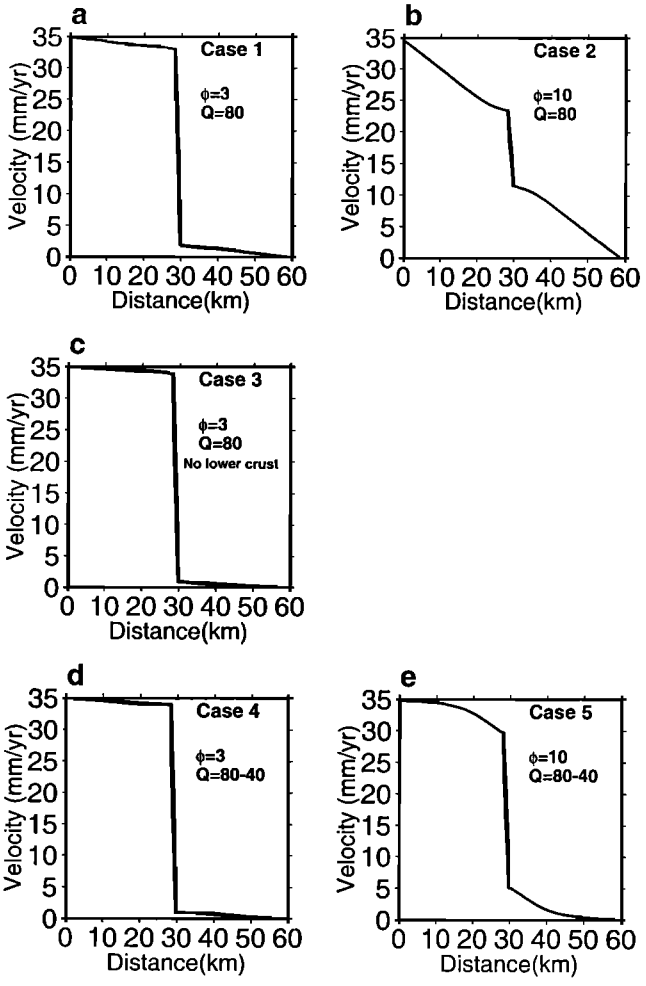

Figure 5. Velocity profiles in y direction along x axis of Figure 2. (a) No lateral heat flow variation, low fault friction. (b) No lateral heat flow variation, moderate fault friction. (c) No lateral heat flow variation, low fault friction, no lower crust. (d) Strong lateral heat flow variation, low fault friction. (e) Strong lateral heat flow variation, moderate fault friction.

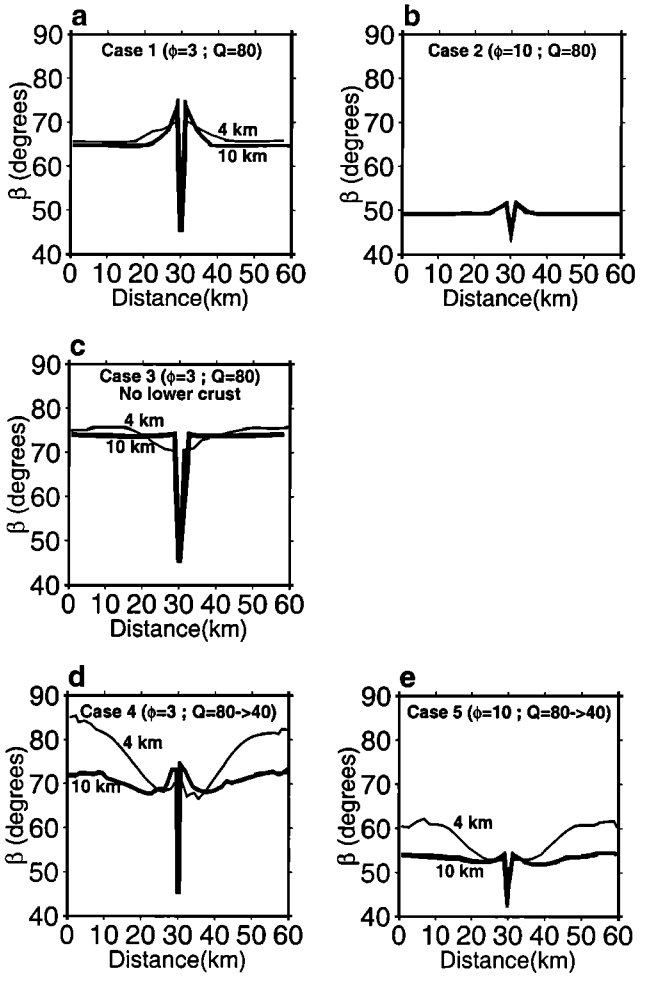

Figure 6. Stress orientation β at 4 km depth (thin line) and at 10 km depth (thick line). (a) No lateral heat flow variation, low fault friction. (b) No lateral heat flow variation, moderate fault friction. (c) No lateral heat flow variation, low fault friction, no lower crust. (d) Strong lateral heat flow variation, low fault friction. (e) Strong lateral heat flow variation, moderate fault friction.

use of a moderate friction (cases 2 and 5) leads to different velocity patterns, depending on the temperature field variations at depth. The fault velocity is only 13 mm yr^{-1} with a constant heat flow (case 2), such that only 37% of the strike parallel velocity is localized on the fault zone. Moreover, the surface velocity gradient $\partial v_y/\partial x$ is clearly reduced in the vicinity of the fault zone. Fault velocity increases when a colder geotherm is used outside the fault zone, and the fault velocity is 25 mm yr^{-1} in case 5. In contrast to case 2, the shape of the velocity profile in case 5 indicates that the deformed zones into the crust are concentrated near the fault zone.

As the SAFS is in transpression, σ_1 is expected to be equal to σ_H, the maximum horizontal principal stress. This enables us to compare the model predictions with the stress data presented in Figure 1. In order to investigate variations of stress orientation we computed the angle β between σ_H and the strike of the fault (y-axis) for two profiles normal to the fault at 4 and 10 km depth. Case 1 shows a clear variation of β with distance to the fault (Figure 6a). Here β is constant and close to 65° at distances > 10 km from the fault and increases to 75° close to the fault; β is 45° within the fault zone itself. Slight differences are seen between depths of 4 and 10 km. These values of β are similar to the values of β computed for the San Francisco Bay near the Hayward fault (Figure 1, inset f) but are clearly smaller than the values found in central California (Figure 1, inset e). Mechanically removing the lower crust in the weak fault model (case 3) leads β to increase to 75° in the entire upper crust (Figure 6c), with minor lateral variations. We therefore see that the effect of removing the lower crust is to increase $\beta \approx 10°$, but it is still not as fault normal as indicated by stress observations in central California (Figure 1, inset e). In this case, β also has a value of 45° within the fault zone, and no significant variation of β with depth is found. A moderately weak fault (case 2, Figure 6b) reduces β in the far field (49°), with almost no variation of this angle near the fault. This clearly does not match observations summarized in Figure 1.

Introducing a laterally variable thermal field induces both lateral and depth variations of β values, especially when a combination of a very weak fault and a strong thermal variation is used (case 4). For this case the combination of a large heat flow variation and a very weak fault zone leads to β values close to 85° at 4 km depth at a distance > 20 km from the fault where the heat flow is low (Figure 6d). Here β is close to 68° in the near field and remains ≈45° in the fault zone. At 10 km depth, β remains close to 70° in the whole crust. Other combinations of other temperatures and fault friction do not yield such high values of β, either at shallow or greater depths (case 5, Figure 6e). The maximum values for cases 1, 2, 3, and 5 remain < 74°. Thus it appears reasonable that the different β values observed in northern and central California may be related to the variation of heat flow with distance from the fault.

3.4. Strain Softening: Cases 6 and 7

Although our modeling involves only a single fault zone, the fault system of central and northern California is obviously more complex (Figure 1). Indeed, parallel strike-slip faults and thrusts also play a role in the deformation of the SAFS. The formation of these faults occurs progressively as the system is deforming, and likely involves many complex processes. As the net effect of these processes may slightly decrease crustal strength, we postulate that the creation of new tectonic features can be simulated using a relation between the frictional properties of the system and the frictional strain that progressively accumulates. To model this, we assume a strain-softening relation between the effective friction angle ϕ_{NC} of the normal crust and the

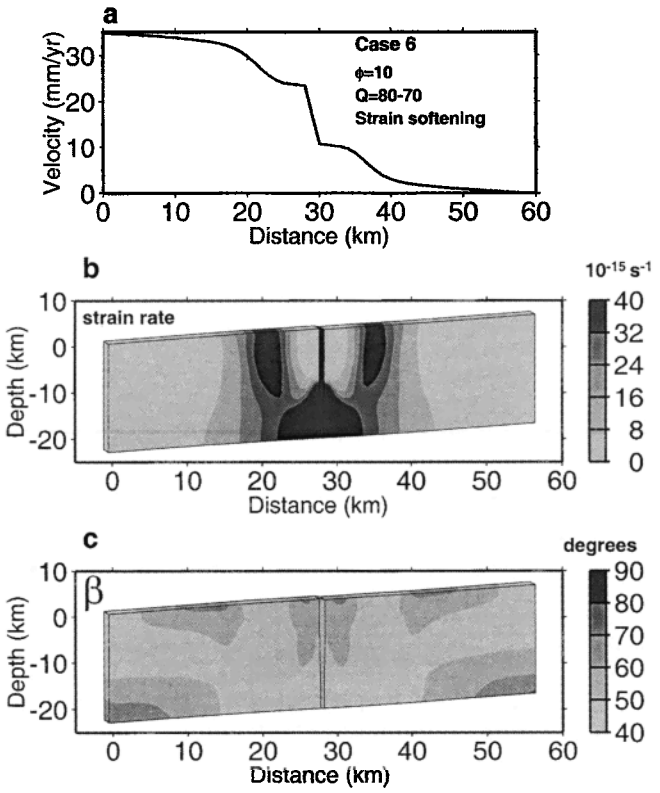

Figure 7. Strain softening, case 6: Moderate lateral heat flow variation and moderate fault friction. (a) Surface velocity profile v_y. (b) Averaged total strain rate $\Delta I_2(d)/\Delta t$. High surface values match high-velocity gradients. (c) Orientation β of the maximum horizontal stress component with respect to the fault axis (y) within the crust. Lower values are within the most deformed areas. Upper values do not exceed 70°.

cumulative plastic strain κ. The friction angle is forced to evolve between an initial angle ϕ_0 when $\kappa = 0$ and a final friction angle ϕ_1 when κ is equal or larger to a limit value κ_c. The relationship between ϕ_{NC} and κ is set following equation (A10) [*Leroy and Ortiz*, 1989]. We choose $\phi_0 = 15°$ as a value for the "normal" crust. Therefore the initial material properties of our strain softening cases are identical to the previous cases. We also postulate that the newly developing shear zones cannot be as weak as a well-developed fault zone like the SAF. Thus we chose $\phi_1 = 10°$ for the minimum value of ϕ_{NC} to allow for moderate weakening. The choice of κ_c is largely arbitrary due to our ignorance of the precise relation between this parameter and the underlying physical processes. We choose a value of 0.03 for κ_c, which is small enough to allow the friction angle to decrease toward its minimum value during the duration of our numerical experiments. We use the same setting as for the variable heat flow cases (4 and 5) to design our experiments. Cases 6 and 7 are therefore directly comparable to previous cases except for allowing the progressive decrease of the friction angle as faults develop in crust. Thus, case 6 involves a weak fault and rapid decrease of heat flow away from the SAF as for case 4, whereas case 7 involves a moderately weak fault and a gradual decrease of heat flow shown in Figure 3b.

The velocity profiles for strike direction (Figure 7a) reveal that the strain localization occurs mainly as parallel shear zones for a moderately weak fault zone (case 6). Strain rates for this case (Figure 7b) show that the combination of a mild heat flow variation in the fault system allows two symmetric vertical shear zones to develop. The computation of β for case 6 on the cross section shows only moderate values between 45° and 70° (Figure 7c), with highest values in the less deformed areas. The weak fault zone model (Case 7) does not show such a distributed velocity gradient across the SAFS (Figure 8a). Rather, the strain rate of this case reveals markedly different secondary faulting as a pair of thrusts dipping toward the fault zone (Figure 8b). These faults cut the upper crust at the transition between the high and low heat flow zone. The computation of stress orientations for case 7 displays very high values of β up to 85°. As for case 4, these values are

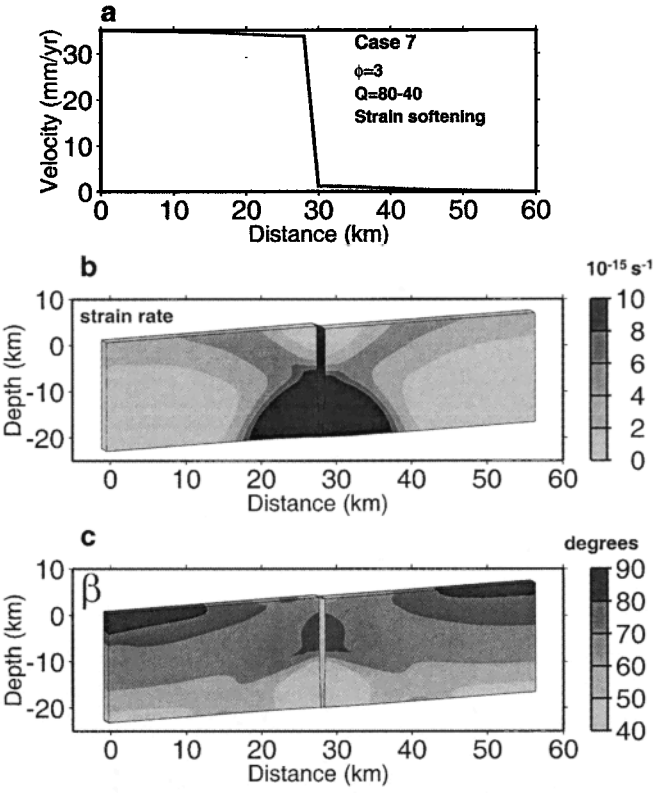

Figure 8. Strain softening, case 7: Strong lateral heat flow variation and low fault friction. (a) Surface velocity profile v_y. (b) Averaged total strain rate $\Delta I_2(d)/\Delta t$. Note that the oblique shear bands correspond to thrust motion and are therefore not associated with a significant v_y variation. (c) Orientation β of the maximum horizontal stress component with respect to the fault axis (y) within the crust. Shallow variation range from 45°in the fault zone to 85° at a distance of 30 km away from the fault; at this distance, β gradually decays with depth until values of 45°at 20 km depth.

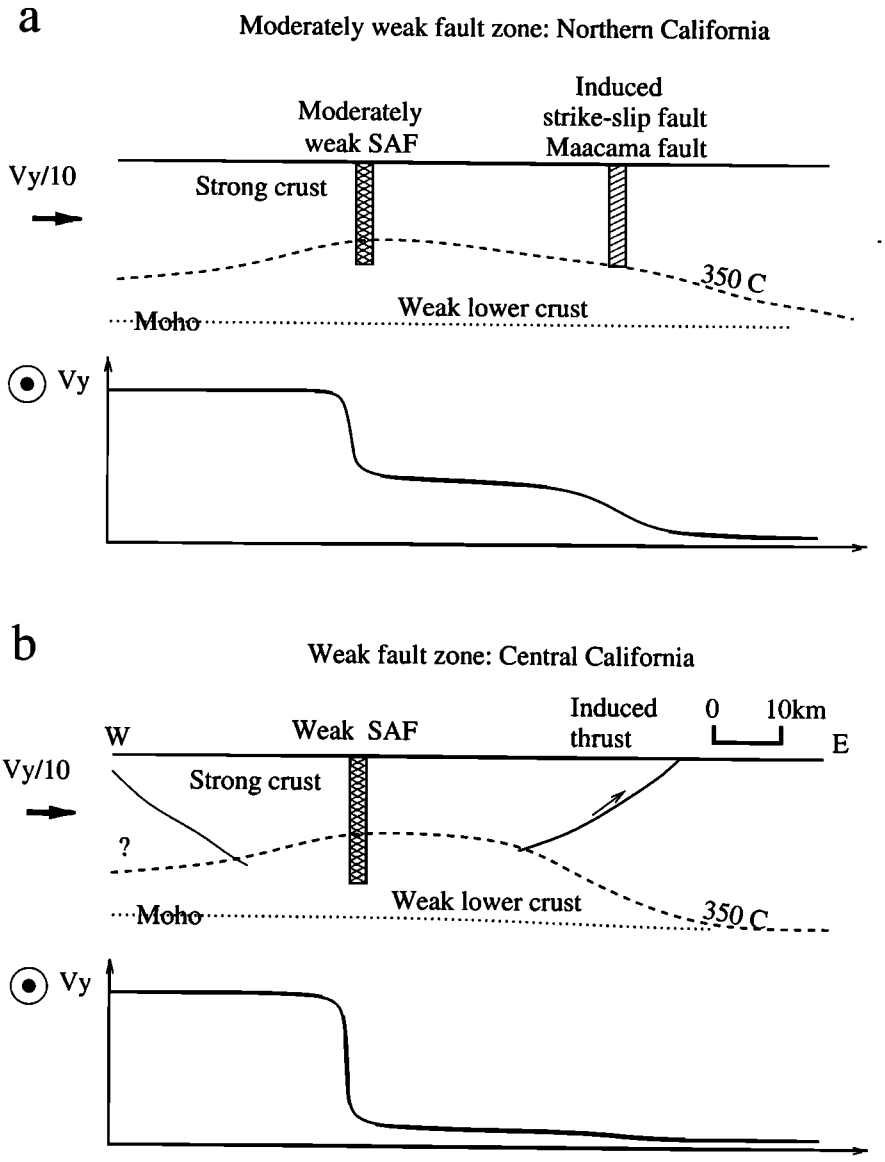

Figure 9. Stress and strain associated with a weakly transpressive margin. (a) Tectonic setting associated with a weak fault zone ($\bar{\tau} \approx 18$ MPa between depths of 0 and 10 km). (b) Tectonic setting associated with a moderately weak fault zone ($\bar{\tau} \approx 55$ MPa between depths of 0 and 10 km).

restricted to the shallow crust in the low heat flow domain. The fact that the parallel faults and the thrust faults are generated for the same shortening rate indicates that the thermal structure and the fault zone rheology plays a dominant role in this structuring process rather than the boundary conditions. More precisely, a thrust develops only in association with a weak fault zone, and a new strike-slip fault zone occurs specifically in conjunction with a moderately weak fault zone (Figure 9).

4. Discussion

4.1. Strain Partitioning and Stress in Central California

Deformation of the SAFS in central California is revealed by geodesy on the creeping segment [e.g., *Lisowski et al.*, 1991] and neotectonic and paleoseismologic studies (Figure 1, inset a). Most of the strike-slip motion between the Pacific plate and the Great Valley occurs within a relatively narrow fault zone (34 mm yr^{-1}). Also, the presence of active thrusts associated with anticline growth (Coalinga and Kettleman Hills) reveals that this section is currently under fault-normal compression [*Page et al.*, 1998]. However, the present compression is relatively minor, with geodetic values of 0.9 $\pm$ 1.8 mm yr^{-1} [*Gordon and Argus*, 1998] and geologic estimates of 1.5–2.0 mm yr^{-1} during the last 15 Myr [*Page et al.*, 1998]. This part of the SAFS is also associated with β close to 90°, especially east of the fault near or within the Great Valley (Figure 1, inset e). Clearly, the only models that account for both this strain and stress orientation are cases 4 and 7, which involve a very weak fault zone and a large lateral heat flow variation.

Although a large scatter in the heat flow data appears in the vicinity of the fault zone (the values around Parkfield range from 54 to 92 mWm^{-2} with a mean value of 74 mW m^{-2} [see *Sass et al.*, 1997]), a large lateral heat flow variation is clearly seen between the SAF and the Great Valley (Figure 1, inset c). A sharp decay of the heat flow anomaly from 80 to 40 mW m^{-2} over 20 km may occur 40 km east of the SAF, roughly corresponding to the easternmost limit of the Coast Ranges. Such a heat flow variation is similar to that used in cases 4, 5, and 7. Moreover, case 7 predicts the development of a thrust in the area where the heat flow decreases most rapidly. It appears therefore that the location of the external thrusts of the SAFS in Central California may mark the limit of high heat flow anomaly in the Coast Ranges.

An important result of cases 4 and 7 is the fact that β is close to 90°at some distance from the fault, but this does not imply the fault itself has no strength at all. This lack of direct relationship is directly linked to the rotation of β with depth in the far field, which is from 85°at 4 km depth to 65°at 15 km depth (Figure 6d). Another important feature of the stress field is that β at shallow depth decreases toward 70°when approaching the fault zone.

Maximum horizontal principal stress orientations compiled by *Zoback et al.* [1987] and *Mount and Suppe* [1987] do not show clear evidence of stress rotations at shallow depths or as a function of fault distance (Figure 1, inset e). However, measurements by *Castillo and Hickman* [1996] in the Carrizo plain east of the SAF show σ_H orientations that do vary with distance from the fault, but the origin of this is unclear. Their data show a relatively abrupt change of stress orientation in the Elk Hills oil field ($\approx$ 20-25 km from the SAF), not a gradual stress rotation with distance.

The other source of information about the directions of principal axis may be provided by the inversion of focal mechanisms. One focal mechanism is not a reliable indicator of stress direction [*McKenzie*, 1969] because the relation between the fault slip and the acting stress is dependent on the friction coefficient of the fault plane. However, the inversion of a group of focal mechanisms with various orientations of P and T axes can be used to yield the corresponding stress field [e.g. *Gephart and Forsyth*, 1984], providing a statistical measure of its consistency. On the basis of this technique, *Hardebeck and Hauksson* [1999] have computed stress inversions along profiles perpendicular to the SAF in southern and central California. Although the authors suggest that stress rotations occur in southern California, *Townend and Zoback* [2001] argue that is not the case. The scarcity of earthquakes in central California does not allow convincing stress rotations to be pointed out for this zone. *Provost and Houston* [2001] find no such rotations near the SAFS just to the south of the area shown in Figure 1.

Any variation of σ_H orientation with depth is difficult to detect. First, wells do not penetrate deep enough in the upper crust to test the predicted variation. Second, focal mechanism inversion needs to be performed in small volumes with enough data in order to compute a reliable stress field at different depths. One possibility is to analyze aftershocks related to moderate to large earthquakes, as has been done for Coalinga, 1982 [*Michael*, 1987], or Loma Prieta, 1989 [*Zoback and Beroza*, 1993], but no systematic variations with depth have been reported.

4.2. Strain Partitioning and Stress in Northern California

The comparison between our model results and the behavior of the SAFS between San Francisco Bay and Point Arena is not straightforward due to the variation of the fault geometries along strike. It is clearly easier to compare the model with the SAFS between the latitude of Point Reyes and Point Arena (38°–39°N) because the main faults (the San Andreas and Maacama faults) are almost parallel. Unfortunately, there are no borehole measurements of σ_H in this region and almost no stress inversions based on groups of focal mechanisms. On the other hand, there are stress orientation data in the east part of the San Francisco bay (Figure 1), but multiple faults of somewhat varied orientations in the bay area (San Gregorio, SAF, Hayward and Calaveras) may complicate interpretations. In the following, we attempt to interpret our results using the geophysical and geological observations coming from these two zones. We mainly use the zone between Point Reyes and Point Arena to discuss the strain observations and the east part of the San Francisco Bay area to discuss stress orientations.

The SAFS heat flow in northern California at 38°–39°N has a mean value of 69 mW m^{-2} [*Lachenbruch and Sass*, 1980]. No significant heat flow variations are observed between the SAF and the Maacama fault. This information seems to be consistent with the maximum seismicity depth in the same zone, which occurs near 12 km [*Sibson*, 1982], except for some segments of the Bartlett Springs fault, where the maximum seismicity depth may locally increase to depths of 18 km [*Castillo and Ellsworth*, 1993]. The heat flow east of the Hayward fault at the latitude of San Francisco decays from 86 mW m^{-2} in the San Francisco bay to 40 mW m^{-2} in the Great Valley 80 km away. (Figure 1, inset d). The heat flow anomaly appears to decay more slowly than in central California. The strain partitioning between the different faults at the latitude of Point Arena and Point Reyes cannot be explained with the cases involving a weak fault and a large heat flow variation because a multi stranded strike-slip fault does not develop (Figure 7b). It seems reasonable to interpret the deformation in this zone in terms of a moderately weak fault as modeled in cases 2, 5 and 6. An obvious limitation of this comparison for northern California is that the strike-slip motion of the SAFS is distributed across

three fault systems, and we only describe one with our model. In addition, the fault zone spacing in our model is $\approx$ 10 km (Figure 7a) but is 40-50 km for the SAF-Maacama-Bartlett Spring fault system. The juvenile fault zones are symmetric with the SAF in our model, whereas the Maacama and Bartlett Spring faults are east of the SAF. Finally, the slip rate of the main fault in case 6 is only 13 mm yr^{-1}, significantly smaller than the 24 mm yr^{-1} slip rate of the SAF at Point Arena.

One way to obtain a better agreement between the observed slip rate of the SAF and the modeled slip rate is probably to lower the friction angle of 10°used to model a moderately weak fault. However, there is a trade off between the friction angle and the thermal model: increasing the friction angle has the same effect as decreasing the lateral heat flow variation. Perhaps, a better way to estimate the frictional properties of the San Andreas-Maacama-Bartlett Spring fault system would be to search for the best combination of friction angles that match the slip rates. However, "tuning" model parameters to match geological conditions has not been the goal of this study.

The disagreement between the natural and modeled fault spacing is more difficult to resolve. The distance between the fault zones in case 6 is $\approx$ 15 km. One possibility is that the intensity of the interaction between the frictional upper crust, the lower crust, and the fault zone could control the spacing between newly formed fault zones. It is interesting to note that the distance between the main parallel strike-slip faults in northern and central California is $\approx$ 50 km everywhere. Another possibility is that the occurrence of sub parallel, strike-slip faults separated by 40-50 km is a genetic feature of the SAFS. Such faults are seen in northernmost California, where the SAFS is only $\approx$ 1 Myr old. If this is the case, perhaps the evolution of sub parallel strike-slip faults separated by $\approx$ 10 km (as shown in Figure 7b) is related to the bifurcation of the SAF into the SAF and Calaveras fault and the subsequent bifurcation of the Calaveras fault into the Calaveras and Hayward faults (Figure 1) rather than the fundamental spacing now observed between them.

The stress orientation data east of the Hayward fault (Figure 1, inset f) indicate $\beta = 70°$ (with respect to the Hayward fault strike). However, β seems to be close to 90°$\approx$ 70 km away from the Hayward fault and decreases at distances of 30 and 50 km from the fault. The interpretation of these data using the modeling results of cases 1–7 is not straightforward. If we use the direction of the Hayward fault as a reference, the trend of β is closely matched by case 4 (Figure 6d). However, the secondary faulting associated with case 4 is a thrust faulting, whereas the Hayward fault is principally a vertical fault, as is the Calaveras. If we had used the direction of the Calaveras fault to compute β, it would have added a constant value of $\approx$ 12° to β. Interpreting the stress orientation data using a moderately weak fault seems appropriate (cases 2 and 5), as the secondary faulting is dominated by a strike-slip faulting (case 6, Figure 7). This also may explain the decrease of β when approaching the Hayward fault. Finally, we must allow for the fact that the stress field of this region is affected by the complex geometry of the SAFS in the San Francisco bay. A detailed 3-D model of this region is probably needed to address this issue.

5. Conclusions

The strain and stress behavior of a vertical strike-slip fault in a transpressional environment such as the central and northern SAFS has been studied using a 3-D finite element model. We have used a rheology that accounts for the partition between the frictional and viscous behavior of the upper and lower crust. We distinguish between the rheology of a "normal crust," which deforms with a high effective friction coefficient, and the rheology of the fault zone, which is markedly weaker. The basic kinematic assumption of the model is that the SAFS is driven by a differential motion of 35 mm yr^{-1} between the Pacific plate and the Great Valley. We also assume that a small amount of transpression (3.5 mm yr^{-1}) is present. The response of the model has been studied with different rheologies for the fault zone and with different thermal structures for the lithosphere.

Our main conclusions can be summarized as follows:

1. Different combinations of geotherms and fault strengths may lead to similar velocity patterns. Velocity data alone are not sufficient to infer the rheological structure of the SAFS. In contrast, the same combinations of parameters indicate distinct variations of σ_H orientations (β).

2. Only significant lateral heat flow variations and low effective friction provide high β values compatible with stress measurements in central California. Vertical variations of β are also predicted, and observing this trend in stress data would be an important constraint on our models.

3. Using frictional strain softening as a proxy for the creation of new faults in the crust adjacent to the strike-slip fault and using a realistic thermal field for central and northern California, we show that different secondary faulting can develop, as summarized in Figure 9. A weak fault zone favors the creation of a pure thrust on the edge of the thermal perturbation (Figure 9b). This thrust absorbs the normal shortening, as observed along the Coalinga/Kettleman anticline trend. A moderately weak fault zone favors the creation of a pair of new strike-slip faults that absorb both the strike and normal motion between plates. This second scenario seems closer to what is observed in northern California (Figure 9a). The fact that these two tectonic styles emerge for the same amount of convergence (3.5 mm yr^{-1}) contradicts the proposition that the amount of convergence controls the tectonic style of a transpressional margin [e.g., *Eaton*, 1990; *Braun and Beaumont*,

1995]. Rather, this result supports the hypothesis that the shear stress along the SAF controls the transition between wrench tectonics and a partitioned deformation [*Mount and Suppe*, 1987].

Finally, we believe that the type of integrated models we have presented here provide a good conceptual framework that tries to satisfy observational data on strain, stress, and heat flow in the vicinity of an actively deforming plate margin. With the underlying foundation of lithospheric rheology our simplified 3-D finite element model shows that the mechanical behavior of the SAFS may be understood in terms of fault zone weakness, the nature of mechanical coupling between the upper and lower crust, and lateral strength variations of the lithosphere resulting from the way in which heat flow varies as a function of distance from the SAFS.

Appendix A

This section is devoted to presenting (1) kinematic and mechanical aspects of the problem, (2) spatial and temporal discretization, (3) stress integration, (4) boundary conditions, and (5) mesh design.

A1. Mechanical Aspects

Let $C_t \subset R^3$ be the space domain (the configuration) of the deformed body at time t. Because large strain and/or large displacement are assumed, C_t is different to the initial configuration C_0 as in small strain formulation. Using a material description, the mechanical problem is to find a tensor field $\sigma(x, y, z)$ and a vector field $v(x, y, z)$ such that:

$$\begin{aligned} \text{div}\ \sigma + f_v &= 0 \quad \text{in } C_t, && \text{(A1)} \\ \frac{D\sigma}{Dt} &= \mathcal{M}(\sigma, d), && \text{(A2)} \\ d &= \frac{1}{2}(\text{grad}\ v + \text{grad}^{\mathrm{T}}\ v), && \text{(A3)} \\ \sigma\, n &= \sigma_s \quad \text{on } \Gamma_f, && \text{(A4)} \\ v &= v_d \quad \text{on } \Gamma_v, && \text{(A5)} \end{aligned}$$

where σ is the Cauchy stress tensor, d is the Eulerian strain rate tensor that is the symmetric part of the velocity gradient, v is the Eulerian velocity field, f_v is the body forces vector, σ_s is the surface stress vector acting on a part Γ_f of the boundary Γ of C_t with outward unit normal n, v_d is the value of the velocity on the part Γ_v of Γ and $D\sigma/Dt$ is an objective stress rate introduced to ensure material invariance through rigid body motion. We use in this work the Jaumann derivative defined as

$$\frac{D\sigma}{Dt} = \dot{\sigma} - \omega\sigma + \sigma\omega, \qquad \text{(A6)}$$

where ω is the local rotation rate that corresponds to the antisymmetric part of the velocity gradient, which is a measure of the spin of the corrotational frame :

$$\omega = \frac{1}{2}(\text{grad}\ v - \text{grad}^{\mathrm{T}}\ v). \qquad \text{(A7)}$$

The functional $\mathcal{M}$ stands for a general constitutive law. Drucker-Prager elastoplasticity is defined by its yield criterion ((3)–(6)) and by the following relations:

$$\begin{aligned} d &= d_e + d_p, && \text{(A8)} \\ \frac{D\sigma}{Dt} &= 2G\, d_e + \lambda\ \text{tr}\ d_e\ I, && \text{(A9)} \\ \sin\phi(\kappa) &= \sin\phi_0, && \text{(A10)} \\ &+ \min[1, \frac{\kappa}{\kappa_c}] \cdot (\sin\phi_1 - \sin\phi_0), \\ \kappa &= I_2(d_p), && \text{(A11)} \end{aligned}$$

where d_e and d_p are the elastic and plastic part of the strain rate tensor d, respectively, and κ is the frictional strain cumulated between 0 and t. Here κ is used as a hardening-softening internal variable. $I_2(\ )$ is the quadratic invariant of a second-order tensor $(\ )$:

$$I_2(\ ) = \sqrt{\frac{3}{2}} \int_0^t \sqrt{(\ ) : (\ )}\ dt. \qquad \text{(A12)}$$

The plastic strain rate d_p is given by the nonassociative flow rule:

$$\begin{aligned} d_p &= \lambda_p \frac{\partial g}{\partial \sigma}, && \text{(A13)} \\ g(\sigma) &= J_2(\sigma) - \theta\bar{\sigma}, && \text{(A14)} \\ \theta &= \frac{6\sin\psi}{3 - \sin\psi}, && \text{(A15)} \end{aligned}$$

where g is the plastic potential, λ_p is the plastic multiplier, and ψ is the dilatancy angle. The plasticity becomes associative if $\psi = \phi$. Assuming that the dilatancy produced by the plastic strain is negligible at a crustal scale, we set the dilatancy angle ψ to zero. As a consequence, the volumetric part of the deformation is only due to elasticity.

A2. Spatial and Temporal Discretization

Using the virtual work principle on the current configuration C_t and assuming a linear finite element approximation v of the velocity field, the discrete form of the equilibrium equations is

$$\mathbf{F_{int}}(\mathbf{V_{qs}}, t) + \mathbf{F_{ext}}(\mathbf{V_{qs}}, t) = 0, \qquad \text{(A16)}$$

where $\mathbf{F_{int}}$, $\mathbf{F_{ext}}$ and $\mathbf{V_{qs}}$ are vectors in R^{3N} (N is the number of nodes of the mesh) which are internal forces, external forces and nodal velocities, respectively.
This non-linear quasi-static system is solved using the dynamic relaxation method [e.g. *Otter et al.*, 1966; *Cundall and Board*, 1988]. The quasi-static solution $\mathbf{V_{qs}}$ is approximated by the solution $\mathbf{V}$ of a pseudo-dynamic problem and the introduction of a user-defined mass matrix $\mathbf{M}$, an acceleration vector $\mathbf{a}$ and a damping force vector $\mathbf{C}$:

$$\mathbf{F_{int}}(\mathbf{V},t) + \mathbf{F_{ext}}(\mathbf{V},t) = \mathbf{M}\cdot\mathbf{a} + \mathbf{C}. \quad \text{(A17)}$$

When these two additional forces become negligible compared to the external and internal forces, the quasi-static solution is reached. This method is coupled with an explicit time discretization scheme:

$$\begin{aligned} \mathbf{a}^{n+1} &= \mathbf{M}^{-1} \\ &\cdot [\mathbf{F_{int}}^n + \mathbf{F_{ext}}^n - \mathbf{C}^n], \quad \text{(A18)} \\ \mathbf{V}^{n+1/2} &= \mathbf{V}^{n-1/2} + \Delta t\, \mathbf{a}^{n+1}, \quad \text{(A19)} \\ \mathbf{X}^{n+1} &= \mathbf{X}^n + \Delta t\, \mathbf{V}^{n+1/2}, \quad \text{(A20)} \end{aligned}$$

where $\mathbf{a}^{n+1}$ is the nodal acceleration vector at time station t^{n+1}, $\mathbf{M}^{-1}$ is the inverse mass matrix, $\mathbf{F_{int}}^n$ and $\mathbf{F_{ext}}^n$ stand for the internal and external forces evaluated at t^n, $\mathbf{V}^{n+1/2}$ is the nodal velocities vector computed at time $t^{n+1/2} = t^n + \frac{1}{2}\Delta t$, $\mathbf{X}^{n+1}$ is the nodal coordinates vector, and Δt is the time step length.

Because the mass matrix $\mathbf{M}$ is chosen to be in diagonal form by element mass concentration, this computation is straightforward and inexpensive. However, the maximum length of the time step Δt is limited by the stability condition of the explicit scheme, which depends on the mass matrix values. As we are only interested by the quasi-static solution, we adjust the mass matrix in such a way [see *Cundall and Board*, 1988] that the stability condition is ensured with a given time step. Moreover, adding the term $\mathbf{C}$ damps the dynamic solution and forces the convergence toward the quasi-static solution. Since this damping term must vanish at the equilibrium, it is chosen to be proportional to out of balance forces:

$$C_i = \alpha_d\, |(F_{int})_i + (F_{ext})_i|\, \frac{(V)_i}{|(V)_i|} \quad \text{(A21)}$$

for $i = 1, 2, ..., 3N$ and $\alpha_d \in]0, 1]$. Practically, $\alpha_d \in [0.5, 0.8]$ appears to be a suitable value.

A3. Stress Integration

Knowing the nodal velocity field $\mathbf{V}$ and the interpolated velocity field $\mathbf{v}$ inside the finite elements, on the current time step, the stress field must be computed on each finite element by integrating the constitutive law. To separate material and kinematic non linearities the constitutive relations are written, at each time step, in a frame that follows the local rotation of the medium [*Dogui*, 1983]. If the Jaumann derivative is used, this rotational frame is the corrotational frame, and the rotation matrix $\mathbf{Q}$ is first computed by solving the differential system:

$$\begin{aligned} \dot{\mathbf{Q}}(t)\mathbf{Q}^{-1}(t) &= \mathbf{w} \quad t \in [t^n, t^{n+1}] \quad \text{(A22)} \\ \mathbf{Q}(t^n) &= \mathbf{I}. \quad \text{(A23)} \end{aligned}$$

According to the isotropy of the functional $\mathcal{M}$ and the definition of the Jaumann derivative, the constitutive law can be rewritten as

$$\dot{\mathbf{\Sigma}} = \mathcal{M}(\mathbf{\Sigma}, \mathbf{D}), \quad \text{(A24)}$$

where $\mathbf{\Sigma} = \mathbf{Q}^T\sigma\,\mathbf{Q}$ and $\mathbf{D} = \mathbf{Q}^T\mathrm{d}\,\mathbf{Q}$ are the unrotated stress and strain rate tensors. Thus the constitutive relations are, at each time step and in the local rotational frame, equivalent to the corresponding infinitesimal relations. Usual time integration algorithms, like elastic prediction-plastic correction methods [e.g., *Ortiz and Simo*, 1986]) are then used to compute the current stress state.

A4. Boundary Conditions

The surface stress vector σ_s imposed on the part Γ_f of the boundary Γ of the body (equation A4) can correspond to two different physical situations in our model (see Figure 2): (1) a hydrostatic pressure normal to the surface at the bottom of the model and (2) an "unknown" load if the surface stress vector is related to the displacement or velocity fields. This is the case for the boundary condition which simulates an infinite structure along strike, as used in this work on the x-z sides of the structure. We want the two x-z sides to follow the same motion since the structure is uniform along the y axis. To achieve this requirement, we compute the velocity change with the constraint that the velocities of two opposites nodes $(1, 2)$ on each x-z sides (points $\mathbf{P_1}$ to $\mathbf{P_2}$ on Figure 2) are the same at the end of each time step. Assuming that $\mathbf{v}_1 = \mathbf{v}_2$ at the previous time step, we compute for each pair of opposite nodes the mean acceleration $\bar{\mathbf{a}}$ for each direction of space:

$$\bar{\mathbf{a}} = \frac{1}{M_1} + M_2\,(M_1\mathbf{a}_1 + M_2\mathbf{a}_2), \quad \text{(A25)}$$

where $\mathbf{a}_i$ is the acceleration of the corresponding nodes:

$$\mathbf{a}_i = \mathbf{M}_i^{-1}[(\mathbf{F}_{ext})_i + (\mathbf{F}_{int})_i - \mathbf{C}_i] \quad i = 1, 2. \quad \text{(A26)}$$

The velocities $\mathbf{v}_i$ are then submitted to the same incremental change:

$$\Delta\mathbf{v}_i = \Delta t\,\bar{\mathbf{a}} \quad i = 1, 2. \quad \text{(A27)}$$

A5. Mesh Design

Two kinds of meshes are used for these experiments in order to detect possible mesh size effects. These tests have been performed for case 1. A coarse mesh with a linear element size of 2 km (5760 elements, case 1) (Figure A1) and a fine mesh with a linear element size of 1 km (22,524 elements, case 1a) have been used. Two mesh widths of 60 (case 1) and 120 km (case 1b) have also been used in order to evaluate the influence of the vicinity of the lateral velocity boundary conditions on the internal strain. The results displayed as horizontal velocity profiles reveal small differences of ≈ 2 mm yr^{-1} between all these different models. The agreement

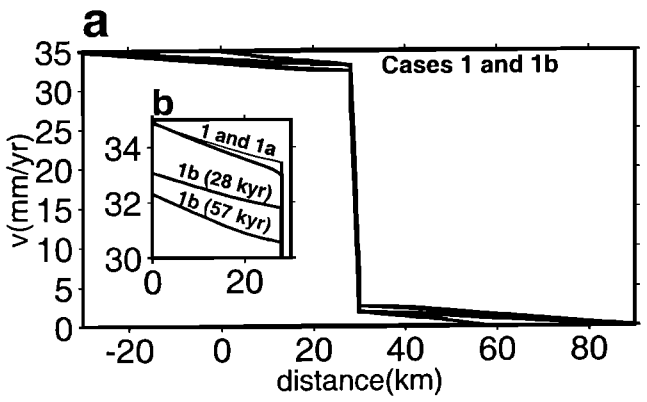

Figure A1. (a) Velocity profile along x axis for two meshes of 60 km width (case 1) and 120 km width (case 1b). (b) Zoom also showing the velocity profile obtained with high-resolution case 1a (thin line).

between the fine and coarse mesh analysis (cases 1 and 1a) is very good (0.2 mm yr^{-1} offset, see Figure A1b) and suggests that the element size is small enough to provide a precise analysis. The difference between the 60 and 120 km width mesh is more significant. This change is due to progressive stress accumulation in the crust that leads to a horizontal shear strain of $\approx$ 2 mm per 30 km for experiments 1 and 1b. Therefore the displacement and the related mean velocity corresponding to this transient behavior directly reflect the mesh width. These slightly different numerical results do not influence the physical interpretation of our results.

Acknowledgments. This research was done while J. Chéry was a visitor at the Department of Geophysics, Stanford University. We thank Wayne Thatcher for a detailed report on an early version of the manuscript. George Thompson and Goetz Bokelmann have also provided useful comments. Reviews by Steve Blair and Greg Lyzenga greatly improved the manuscript.

References

Argus, D., and R. Gordon, Current Sierra Nevada-North America motion from very long baseline interferometry: Implications for the kinematics of the western United States, *Geology*, *19*, 1085–1088, 1991.

Atwater, T., Implications of plate tectonics for the cenozoic tectonic evolution of western North America, *Geol. Soc. Am. Bull.*, *81*, 3513–3536, 1970.

Atwater, T., and J. Stock, Pacific-North America plate tectonics and neogene southwestern United States: An update, *Int. Geol. Rev.*, *40*, 375–402, 1998.

Bird, P., and X. Kong, Computer simulations of California tectonics confirm very low strength of major faults, *Geol. Soc. Am. Bull.*, *106*, 159–174, 1994.

Brace, W., and D. Kohlstedt, Limits on lithospheric stress imposed by laboratory experiments, *J. Geophys. Res.*, *85*, 6248–6252, 1980.

Braun, J., and C. Beaumont, Three-dimensional numerical experiments of strain partitioning at oblique plate boundaries: Implications for contrasting tectonic styles in the southern Coast Ranges, California, and central South Island, New Zealand, *J. Geophys. Res.*, *100*, 18,059–18,074, 1995.

Brown, R. D. J., Quaternary deformation, in *The San Andreas Fault System, California*, edited by R. Wallace, *U.S. Geol. Surv. Prof. Pap.*, 1515, 83–114, 1990.

Brune, J. N., T. L. Henyey, and R. F. Roy, Heat flow, stress, and rate of slip along the San Andreas fault, California, *J. Geophys. Res.*, *74*, 3821–3827, 1969.

Byerlee, J., Friction of rocks, *Pure Appl. Geophys.*, *116*, 615–626, 1978.

Carslaw, H., and J. Jaeger, *Conduction of Heat in Solids*, Oxford Univ. Press, New York, 1959.

Castillo, D., and W. Ellsworth, Seismotectonics of the San Andreas fault system between Point Arena and Cape Mendocino in northern California: Implications for the development and evolution of a young transform, *J. Geophys. Res.*, *98*, 6543–6560, 1993.

Castillo, D., and S. Hickman, Near-field stress and pore pressure observations along the Carrizo plain segment of the San Andreas fault in California, *AAPG Abstr. Programs*, *5*, 24, 1996.

Cundall, P. A., and M. Board, A microcomputer program for modelling large-strain plasticity problems, in 6th *International Conference in Numerical Methods in Geomechanics*, pp. 2101–2108, edited by G. Swoboda, A.A. Balkema, Brookfield, Vt., 1988.

DeMets, C., R. Gordon, D. Argus, and S. Stein, Current plate motions, *Geophys. J. Inter.*, *101*, 425–478, 1990.

Dhatt, G., and G. Thouzot, *Une Présentation de la Méthode des Éléments Finis*, Maloine, Paris, 1981.

Dickinson, W., and B. Wernicke, Reconciliation of San Andreas slip discrepancy by a combination of interior Basin and Range extension and transrotation near the coast, *Geology*, *25*, 663–665, 1997.

Dixon, T. H., S. Robaudo, J. Lee, and M. C. Reheis, Constraints on present-day Basin and Range deformation from space geodesy, *Tectonics*, *14*, 755–772, 1995.

Dogui, A., Contribution à l'étude de l'écrouissage isotrope et anisotrope en grandes déformations élastoplastiques, thèse de doctorat, Univ. Pierre et Marie Curie, Paris, 1983.

Eaton, J., Regional seismotectonic model for the southern Coast Ranges, in *The Coalinga, California, Earthquake of May 2, 1983*, edited by M. Rymer and W. Ellsworth, *U.S. Geol. Surv. Prof. Pap.*, *1487*, 83–114, 1990.

Gephart, J., and D. Forsyth, An improved method for determining the regional stress tensor using earthquake focal mechanism data: Application to the San Fernando sequence, *J. Geophys. Res.*, *89*, 9305–9320, 1984.

Gordon, R. G., and D. F. Argus, Present tectonic motion across the coast ranges and San Andreas fault system in central California, *Eos Trans. AGU*, *79* (45), Fall Meet. Suppl., F204, 1998.

Hardebeck, J., and E. Hauksson, Role of fluids in faulting inferred from stress field signatures, *Science*, *285*, 236–239, 1999.

Hinton, D., and E. Owen, *Finite Elements in Plasticity: Theory and Practice*, Pineridge, Swansea, Wales, 1980.

Kirby, S., Rocks mechanics observations pertinent to the rheology of the lithosphere and the localization of strain along shear zones, *Tectonophysics*, *119*, 1–27, 1985.

Lachenbruch, A., and J. Sass, Thermo-mechanical aspects of the San Andreas fault system, in *Proceedings of the Conference on the Tectonic Problem on the San Andreas Fault System*, pp. 192–205, Stanford Univ. Press, Stanford, Calif., 1973.

Lachenbruch, A., and J. Sass, Heat flow and energetics of the San Andreas fault zone, *J. Geophys. Res.*, *85*, 6185–6222, 1980.

Lachenbruch, A., and J. Sass, Heat flow from Cajon Pass,

fault strength, and tectonic implications, *J. Geophys. Res.*, *97*, 4995–5015, 1992.

Leroy, Y., and M. Ortiz, Finite element analysis of strain localization in frictional materials, *Int. J. Numer. Anal. Methods Geomech.*, *13*, 53–74, 1989.

Lisowski, M., J. C. Savage, and W. H. Prescott, The velocity field along the San Andreas fault in central and southern California, *J. Geophys. Res.*, *96*, 8369–8389, 1991.

McKenzie, D., The relationship between fault plane solution for earthquakes and the directions of the principal stresses, *Bull. Seismol. Soc. Am.*, *59*, 591–601, 1969.

Michael, A., Stress rotation during the Coalinga aftershock sequence, *J. Geophys. Res.*, *92*, 7963–7979, 1987.

Miller, D., Distributed shear, rotation, and partitioned strain along the San Andreas fault, central California, *Geology*, *26*, 867–870, 1998.

Mount, V., and J. Suppe, State of stress near the San Andreas fault: Implications for wrench tectonics, *Geology*, *15*, 1143–1146, 1987.

Namson, J., and T. Davis, Structural transect of the western Transverse Ranges, California: Implications for lithospheric kinematics and seismic risk evaluation, *Geology*, *16*, 675–679, 1988.

Ortiz, M., and J. Simo, An analysis of a new class of integration algorithms for elastoplastic constitutive relations, *Int. J. Numer. Methods. Eng.*, *23*, 353–366, 1986.

Otter, J. R. H., A. C. Cassell, and R. E. Hobbs, Dynamic relaxation., *Proc. Inst. Civ. Eng.*, *35*, 633–656, 1966.

Page, B., G. Thompson, and R. Coleman, Late Cenozoic tectonics of the central and southern Coast Ranges, *Geol. Soc. Am. Bull.*, *110*, 846–876, 1998.

Provost, A.-S., and H. Houston, Orientation of the stress field surrounding the creeping section of the San Andreas fault: Evidence for a narrow mechanically weak fault zone, *J. Geophys. Res.*, *106*, 11,373–11,386, 2001.

Rice, J., Fault stress states, pore pressure distributions, and the weakness of the San Andreas fault, in *Fault Mechanics and Transport Properties of Rocks*, pp. 475–503, Academic, San Diego, Calif., 1992.

Sass, J., C. Williams, A. Lachenbruch, S. Galanis Jr., and F. Grubb, Thermal regime of the San Andreas fault near Parkfield, California, *J. Geophys. Res.*, *102*, 27,575–27,585, 1997.

Sibson, R., Fault zone model, heat flow, and the depth distribution of earthquakes in the continental crust of the united states, *Bull. Seismol. Soc. Am.*, *72*, 151–163, 1982.

Strehlau, J., and R. Meissner, Estimation of crustal viscosities and shear stresses from an extrapolation of experimental steady state flow data, in *Composition, Structure, and Dynamics of the Lithosphere-Asthenosphere System, Geodyn. Ser.* vol. 16, edited by K. Fuchs and C. Froidevaux, pp. 69–87, AGU, Washington, D.C., 1987.

Teyssier, C., and B. Tikoff, Strike-slip partitioned transpression of the San Andreas fault system: A lithospheric scale approach, in *Continental Transpressional and Transtensional Tectonics*, edited by R. E. Holdsworth, R. A. Strachan, and J. F. Dewey, *Geol. Soc. Spec. Pub.*, *135*, 143–158, 1998.

Thatcher, W., and P. England, Ductile shear zones beneath strike-slip faults: implications for the thermomecanics of the San Andreas fault zone, *J. Geophys. Res.*, *103*, 891–905, 1998.

Thatcher, W., G. Foulger, B. Julian, J. Svarc, E. Quilty, and G. Bawden, Present-day deformation across the Basin and Range province, western United States, *Science*, *283*, 1714–1718, 1999.

Thompson, G. A., California coast ranges tectonics in the light of geophysical constraints: A tribute to Ben Page, *Int. Geol. Rev.*, *41*, 383–390, 1999.

Townend, J., and M. D. Zoback, How faulting keeps the crust strong, *Geology*, *28*, 399–402, 2000.

Townend, J., and M. D. Zoback, Implications of earthquake focal plane mechanisms for the frictional strength of the San Andreas fault, in *The Nature and Tectonic Significance of Fault Zone Weakening*, edited by J. F. Maggloughlin, and R. J. Knipe, *Geol. Soc. Spec. Pub.*, *186*, 13–21, 2001.

USGS Working Group, Database of potential sources for earthquakes larger than magnitude 6 in northern California, *U.S. Geol. Surv. Open File Rep.*, *96-705*, 1996.

Wilcox, R., T. Harding, and D. Seely, Basic wrench tectonics, *AAPG Bull.*, *57*, 74–96, 1973.

Zienkiewicz, O., *The Finite Element Method*, McGraw-Hill, New York, 1977.

Zoback, M. D., and G. Beroza, Evidence for near-frictionless faulting in the 1989 (M 6.9) Loma Prieta, California earthquake and its aftershocks, *Geology*, *21*, 181–185, 1993.

Zoback, M. D., et al., New evidence of the state of stress of the San Andreas fault system, *Science*, *238*, 1105–1111, 1987.

Zoback, M. L., R. C. Jachens, and J. A. Olsen, Abrupt along-strike change in tectonic style: San Andreas fault zone, San Fransisco Peninsula, *J. Geophys. Res.*, *104*, 10,719–10,742, 1999.

J. Chéry, Laboratoire de Géophysique, Tectonique et Sédimentologie, Université de Montpellier II, 34095 Montpellier, France. (jean@dstu.univ-montp2.fr)

R. Hassani, Laboratoire d'Instrumentation Géophysique, Université de Savoie, Le Chablais, 73376 Le Bourget-du-Lac, France. (riad.hassani@univ-savoie.fr)

M. D. Zoback, Department of Geophysics, Stanford University, Stanford, CA 94305, USA. (zoback@pangea.stanford.edu)

(Received July 12, 2000; revised December 15, 2000; accepted April 21, 2001.)